Korean J. Chem. Eng., 39(10), 2713-2724 (2022)
DOI: 10.1007/s11814-022-1140-1

pISSN: 0256-1115
eISSN: 1975-7220

Novel heterojunction magnetic composite MIL-53 (Fe)/$ZnFe_2O_4$: Synthesis and photocatalytic pollutant degradation

Mahnaz Mohebali Nejadian*,, Niyaz Mohammad Mahmoodi*,†, Cyrus Ghotbi**, and Farhad Khorasheh****

*Department of Environmental Research, Institute for Color Science and Technology, Tehran, Iran
**Department of Chemical and Petroleum Engineering, Sharif University of Technology, Tehran, Iran
(*Received 24 January 2022 • Revised 4 April 2022 • Accepted 6 April 2022*)

Abstract−A new magnetic composite was synthesized by integration of $ZnFe_2O_4$ and MIL-53(Fe) micro-rods by a solvothermal method. This composite served as a heterogeneous catalyst to overcome the high electron-hole recombination rates of $ZnFe_2O_4$ and to enhance the degradation of Direct Red 23 under visible light irradiation. Different analytical techniques, including XRD, FTIR, SEM, DRS, VSM, and PL, were employed to characterize the synthesized heterojunction nanocomposite and to evaluate its photocatalytic activity. The $ZnFe_2O_4$/MIL-53(Fe)/Vis-light system resulted in significantly higher dye degradation as compared with pristine $ZnFe_2O_4$ and MIL-53(Fe) semiconductors at the optimum pH of 3.1 and irradiation time of 120 minutes. Moreover, the composite exhibited high magnetization property that led to easy collection and recovery from effluent solution. It also retained its durability and stability after five cycles. The photo-generated hole was found to be the primary dye destruction agent as specified by the scavenger test.

Keywords: Heterojunction Composite, Magnetic Metal-organic Framework, Wastewater, Photocatalytic Pollutant Degradation

INTRODUCTION

The increase in demand for clean water in recent decades has resulted in significant research activity on development of efficient and economical technologies for water treatment [1-3]. Diverse pollutions, such as industrial dyes, pharmaceuticals and personal care products (PPCPs), textile effluents, insecticides, and domestic wastewater, enter the surface water as well as ground water [4]. Most of these pollutants are synthetic organic compounds that directly or indirectly affect human lives [5,6]. Among synthetic dyes, azo dyes are more diverse and are commonly used in food, paper, leather, and paint industries [7]. The azo dyes also demonstrate excellent chemical stability because of the π-π conjunction effects between the aromatic rings and the azo group (-N=N-). They are usually non-biodegradable and are resistant to decay [2,8,9]. Direct Red 23 (DR-23) is a common anionic and azo dye used in different industries and its chemical structure is presented in Fig. 1. Advanced oxidization process (AOP) is an efficient, eco-friendly, and economical technology to remove pollutants such as dye from industrial effluents [9-11]. Among various AOPs, a heterogeneous photocatalyst process using visible light is regarded as a promising approach for treating wastewaters containing DR-23 azo dye [12]. The aromatic amines produced from dye degradation can be further degraded by the photocatalyst into carbon dioxide, water, and inorganic ions [13].

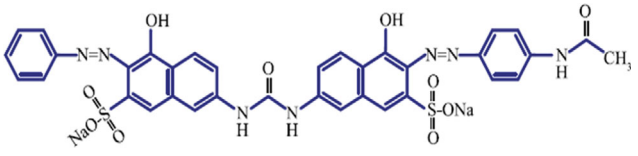

Fig. 1. Chemical structure of azo dye Direct Red 23.

Magnetic photocatalysts allow for easy removal from the reaction effluent when a magnetic field is applied. Recent investigations have demonstrated that one of the n-type magnetic semiconductor, the spinel zinc ferrite ($ZnFe_2O_4$) structured nanoparticles (NPs) with narrow bandgap energy of approximately 1.94 eV and nontoxic nature, natural abundance, inexpensive, environmental friendliness, and good ferromagnetism properties, can be successfully employed as a photocatalyst under visible light irradiation [11,14-16].

As a monophasic semiconductor material, however, zinc ferrite has a low photo response because of its narrow bandgap that leads to fast recombination of charge carriers, thus exhibiting low photocatalytic efficiency. Combining two or more semiconductors with suitable band edges to compose a heterojunction structure can improve their photocatalytic performance. Semiconductors with different bandgaps and positions could also exhibit possible synergistic effects that would facilitate the separation of electron and hole pairs and reduce recombination of the photogenerated carriers in the semiconductor [14]. Due to narrow bandgap of the $ZnFe_2O_4$ and its high recombination rate, it has been modified by other compounds and semiconductors to improve its photocatalytic efficiency. $ZnFe_2O_4$/ZnO [17], $ZnFe_2O_4$/Fe_3O_4/Ag [18], $ZnFe_2O_4$/$SrFe_{12}O_{19}$ [19], $ZnFe_2O_4$/BN [20], $ZnFe_2O_4$-C_3N_4 [21], and Fe_2O_3/$ZnFe_2O_4$/ZnO [22] have been synthesized and used as photocatalysts.

Metal-organic frameworks (MOFs) have attracted considerable

†To whom correspondence should be addressed.
E-mail: mahmoodi@icrc.ac.ir, nm_mahmoodi@aut.ac.ir

attention as microporous compounds with photocatalytic ability and ultrahigh surface area, tunable pore size, and well-defined porosity. MOFs have been used in various applications, including molecular sensing, gas storage (CO_2, H_2S, CH_4), drug delivery, and heterogeneous photocatalysis [23-25]. For MOFs including the MIL series and MOF-5 that are synthesized from transition metals and oxygen-containing ligands, the bonding between transition metals and oxygen of the ligands leads to metal oxide clusters (Fe-O, Cr-O, Ti-O, and Zn-O) that can display photocatalytic activity when exposed to light irradiation [26-28]. MOFs are built from periodic lattice structures in which cation clusters are interconnected by the organic ligand with benzene aromatic rings by coordination bonds [28]. Flexible MOFs have attracted attention because they combine the crystalline order of the coordination framework with structural flexibility. They can also respond to chemical or physical excitation including light, heat, or the introduction of guest molecules in pores [29]. Only about one hundred of some 20,000 reported MOFs demonstrate the "breathing effect" or flexible behavior in response to the external excitation. Such MOFs are better candidates for applications that require selective adsorption properties [30]. Guest molecules can easily fit inside the framework while the crystallinity and atomic structure are preserved [31,32]. MIL-53, a well-known MOF for its breath effect and high flexibility, has become very popular for different applications in the last two decades. Fe(III) based MIL-53 has a three-dimensional porous solid structure constructed by infinite one-dimensional channel linkage of -Fe-O-O-Fe-O-Fe- as metal cluster or metal nodes. These metal clusters are named secondary building units (SBU) with bis-bidentate terephthalate (BDC) as ligand [33,34]. The Fe-based MIL-53, like TiO_2 whose conduction band is made of empty Ti 3d orbitals, contains iron transition metal nodes and the empty metal d orbitals mix with LUMO of the organic ligands to form the conduction band [22]. Furthermore, due to the presence of Fe in MIL-53 structure, it accelerates the Fenton-like process [23]. The presence of carboxylate group in terephthalic acid ligand is also beneficial for enhancement of photocatalytic efficiency. These carboxylates agents form complexes with Fe(III) by ligand-to-metal charge transfer (LMCT) process that are extremely stable in acidic media up to neutral pH [5,35,36]. They are also strong electron donors that facilitate the electron transfer and the production of hydroxyl radicals in the photocatalytic reaction mechanism [5]. Iron-terephthalate MIL-53 with a larger bandgap than $ZnFe_2O_4$ is therefore a suitable candidate to combine with spinel zinc ferrite semiconductor to enhance the charge separations and overall photocatalytic activity [36].

The solvothermal synthesis, characterization, and evaluation of photocatalytic activity of magnetic composite ($ZnFe_2O_4$/MIL-53) were the goals of the present study. According to the previous articles, the loading of zinc ferrite on MIL-53 to synthesize novel magnetic composite ($ZnFe_2O_4$/MIL-53(Fe)) has not been reported so far. Furthermore, no detailed investigation has been fulfilled on the degradation of Direct Red 23 using the photocatalytic mechanism. The synthesized photocatalyst was characterized by X-ray powder diffraction (XRD), FTIR, field emission scanning electron microscopy (SEM), EDX, UV-Vis diffuse reflectance spectrum (DRS), and vibrating sample magnetometer (VSM). The synthesized heterojunction magnetic composite was employed as a photocatalyst for degradation of Direct Red 23 under visible light irradiation using a 100W LED lamp. The influence of operating parameters (catalyst dosage, dye concentration, pH of solution) on photocatalytic activity was also investigated. Radical species present in the reaction medium were identified by scavenger tests and a possible mechanism for the photocatalytic degradation was proposed.

MATERIALS AND METHODS

1. Materials

Zinc (II) dihydrate acetate ($Zn(AC)_2{\cdot}2H_2O$), Iron (III) hexahydrate chloride ($FeCl_3{\cdot}6H_2O$), and 1,4-benzene dicarboxylic acid (Terephthalic acid, $C_8H_6O_4$) were used as precursors for the synthesis of zinc ferrite ($ZnFe_2O_4$: ZFO) and M53Fe MOF. Ethanol and N, N-dimethyl formamide (DMF, C_3H_7NO) were used as solvents in the synthesis of ZFO, M53Fe, and the magnetic composite photocatalyst (ZFO/M53Fe). Sodium hydroxide (NaOH) was used for pH adjustment. Ethanol and deionized water were used to wash the as-synthesized materials. Direct Red 23 (DR23) was used as an organic pollutant in the photocatalytic activity tests. EDTA-4Na, L-ascorbic acid, and isopropanol alcohol were used for the quench tests. All materials were acquired from Merck Germany and used without pre-treatment.

2. Synthesis

2-1. Synthesis of $ZnFe_2O_4$ Nanoparticles

$ZnFe_2O_4$ was synthesized by a solvothermal method reported in the previous literature [37]. 0.5543 g of $Zn(Ac)_2{\cdot}2H_2O$ and 1.3652 g of $FeCl_3{\cdot}6H_2O$ were dissolved in 20 ml ethanol; this solution was named A. Then 2.0833 g of NaOH was dissolved in 20 ml of deionized water (solution B) for pH adjustment. Solution B was slowly added by a burette to solution A under magnetic stirring. The mixed solution was stirred for 30 minutes until the appearance of a uniform suspension. The mixture was then transferred to a 50 ml Teflon -lined autoclave and heated at 180 °C for 24 hours. The autoclave was then allowed to cool to room temperature. A dark brown sediment was readily collected by a magnet and subsequently washed with ethanol and deionized water three times while in a shaker. The solid brown pristine $ZnFe_2O_4$ powders (ZFO) was obtained after drying at 80 °C for 6 hours.

2-2. Synthesis of MIL-53(Fe) and Magnetic Composite (MC) ZFO/M53Fe

The synthesis of the magnetic composite was based on the solvothermal method reported in the literature [38]. 0.3 g of ZFO, 0.8115 g of $FeCl_3{\cdot}6H_2O$, and 0.498 g of Benzene-1,4-dioic acid (BDC) were added to 15 ml of N, N-dimethylformamide. After ultra-sonication for about 20 minutes, the resulting brown mixture was placed in a 50 ml Teflon-lined stainless-steel autoclave and heated for 12 hours at 150 °C. The autoclave was allowed to cool to room temperature, and the autoclave content was then centrifuged at 7,200 rpm for 6 minutes. The product was suspended in 200 ml of distilled water overnight to remove the solvent. The suspended particles were then collected by a strong magnet and placed on a shaker with a small amount of distilled water. The shaking procedure was repeated two or three times. The sample was subsequently dried in a vacuum oven for 24 hours at 60 °C. Pristine MIL-53 (M53Fe)

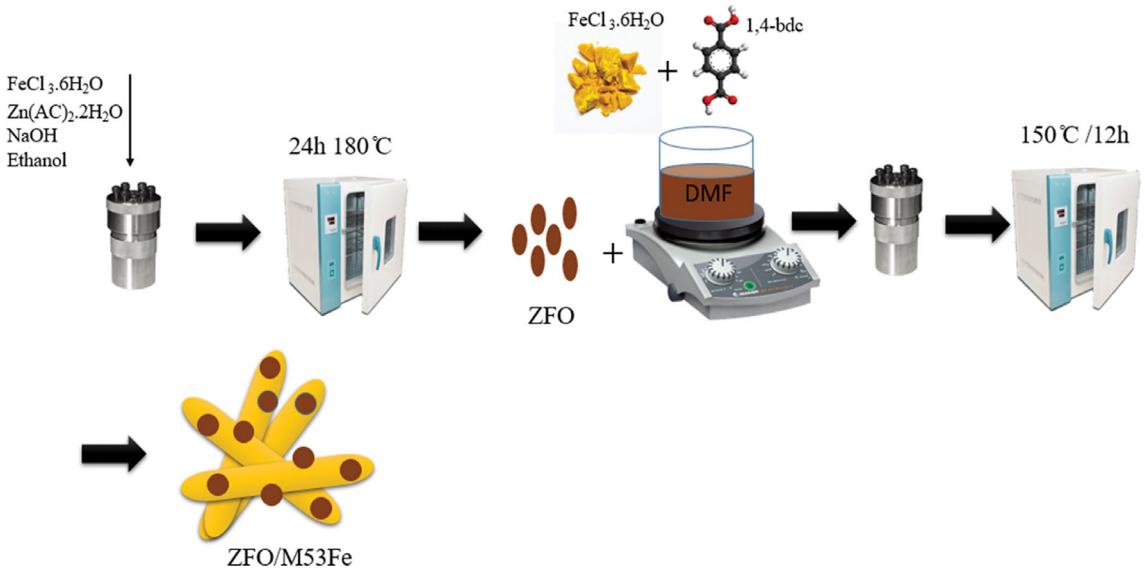

Fig. 2. Schematic of the synthesis of magnetic composite ZFO/M53Fe.

was synthesized in a similar manner without the initial addition of $ZnFe_2O_4$. A schematic of the synthesis procedure for the magnetic composite is illustrated in Fig. 2.

3. Characterization

FTIR analysis was performed using a Perkin-Elmer spectrophotometer to determine functional groups of the synthesized catalysts. Field-emission-Scanning electron microscopy (FE-SEM) and energy-dispersive X-ray spectroscopy (EDX) analyses were performed using TeScan - Mira 3 model electron microscope. XRD analyses were carried out using X-ray diffraction PANalytical 2009 instrument (Netherlands). DRS-UV-Visible Spectroscopy was performed to evaluate the band gap and photoluminescence (PL) analysis was carried out to examine the recombination rates of the synthesized photocatalysts. A vibrating sample magnetometer was used to examine the magnetic properties of the photocatalysts. The DR23 concentration in the aqueous phase was determined by single beam UV-Vis spectrophotometer (CECIL 2000SERIES).

4. Photocatalytic Activity Tests

The photocatalyst activity for dye degradation was investigated using a homemade reaction system [39]. 100 ml solution of (10 mg/l) DR23 dye concentration was prepared. The initial solution pH was 5.6 without pH adjustment. 1 M Hydrochloric acid was added dropwise to reach the desired solution pH of 3.1. For other pH values (5, 7, and 9), the desired pH was obtained by addition of hydrochloric acid or sodium hydroxide solutions. The initial solution containing a certain amount of as-synthesized photocatalyst (optimum concentration of 50 mg/l) was stirred mechanically by a magnet for 1 hour in dark to obtain adsorption-desorption equilibrium [40]. The 100W LED lamp was then turned on and at the set intervals of 30 minutes, 3 ml sample was withdrawn from the reactor by a syringe. The sample was then centrifuged and UV absorbance at 503 nm was used to determine the Direct Red 23

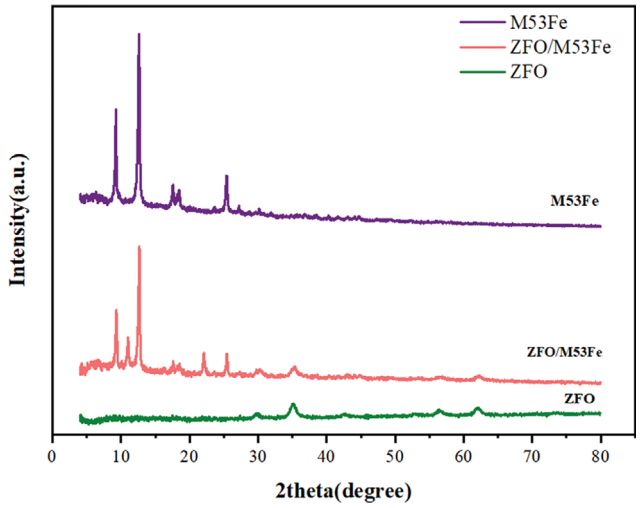

Fig. 3. XRD patterns of three photocatalyst samples.

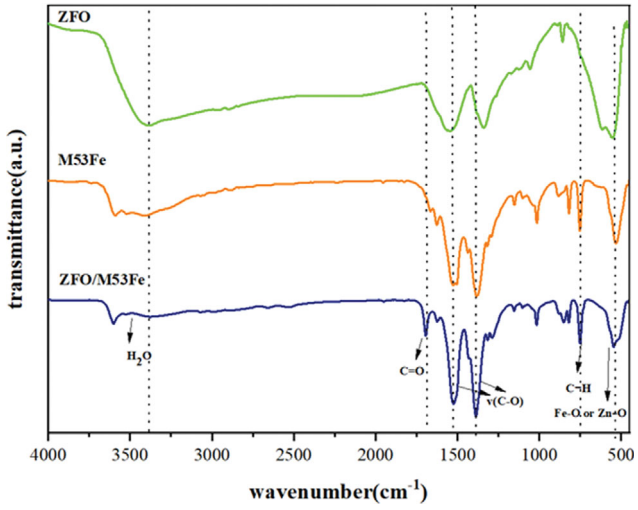

Fig. 4. FTIR spectra of different photocatalysts.

residual concentration [41]. Percentage of DR23 degradation was calculated by Eq. (1) [42]:

$$\% \text{ degradation} = \frac{C_0 - C}{C_0} \times 100 \quad (1)$$

where C_0 and C are the initial and final concentrations of DR23, respectively.

RESULTS AND DISCUSSION

1. Photocatalyst Characterization

The XRD patterns for ZFO, M53Fe, and ZFO/M53Fe are presented in Fig. 3 for 2θ range of 5-80°. Sharp and distinguished peaks for MIL-53 (Fe) appear at 2θ values of 9.24, 12.63, 17.59, 18.49, 25.41, and 30.16 in accordance with the literature [43,44]. The XRD peaks for the cubic phase of ZFO appearing at 2θ values of 29.93, 35.10, 42.63, 52.98, 56.44, and 62.19 can be attributed to crystal plane of (220), (311), (400), (422), (511), and (440), respectively. They are in excellent agreement with what is reported in the literature [19,38,45,46]. The XRD pattern of synthesized ZFO/M53Fe has two additional characteristic peaks located at 2θ value of about 11.09 and 22 as compared with the peaks for pure M53Fe and ZFO photocatalysts.

Owing to the high flexibility of MIL-53 framework and its intrin-

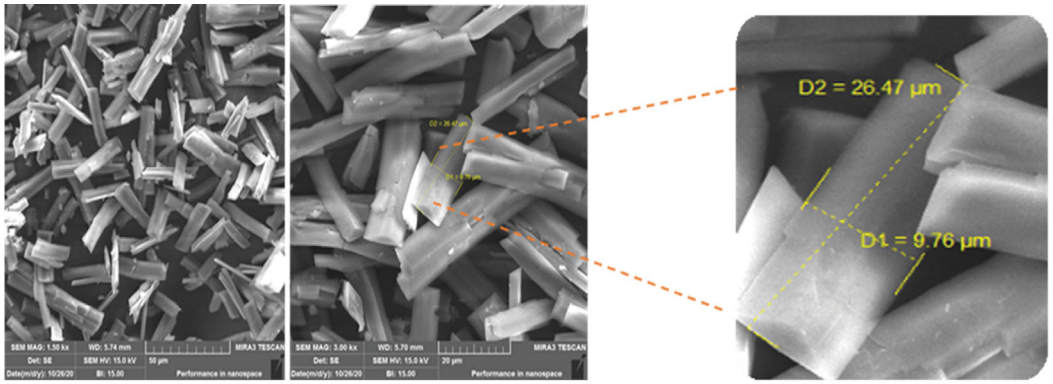

(a)

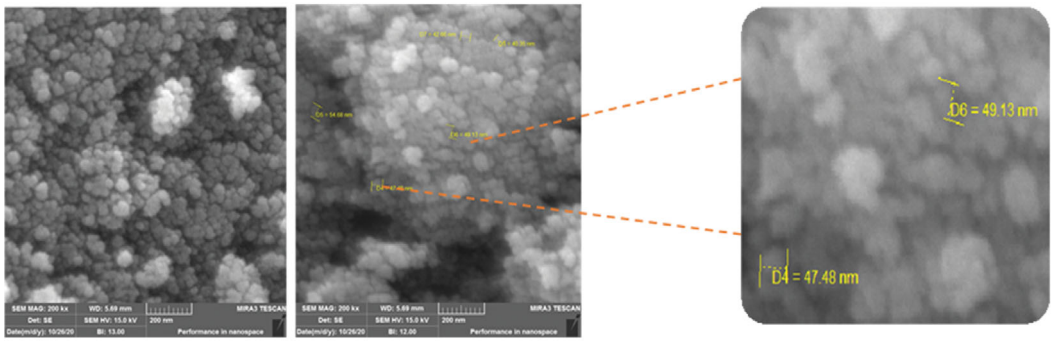

(b)

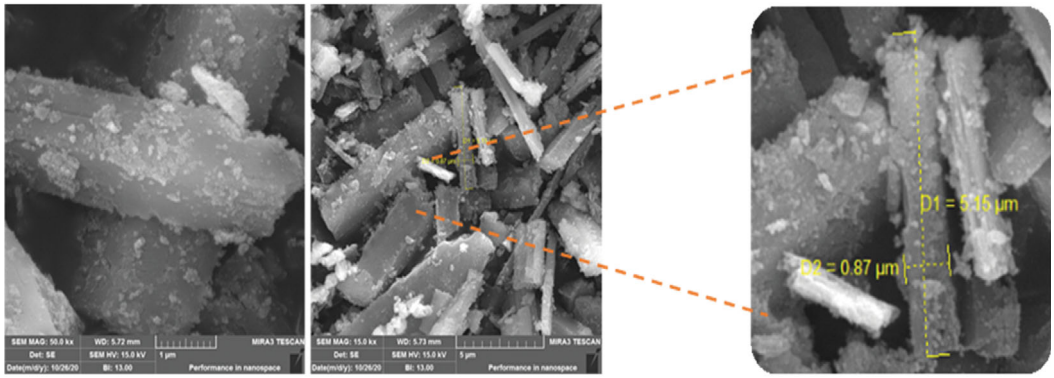

(c)

Fig. 5. FE-SEM images of (a) M53Fe, (b) ZFO, and (c) ZFO/M53Fe.

sic "breathing effect", the guest molecules can be embedded in the pores of the framework's [31,32]. It has been demonstrated that the M53Fe framework can have four different orientations (a, b, c, d), thus causing shifts in XRD peaks [46]. In the present investigation, the synthesized MC had XRD pattern corresponding to orientations b and c that were formed simultaneously, suggesting the successful synthesis of ZFO/M53Fe MC [47,48]. The crystallite sizes were evaluated using the Debye- Scherrer equation [49] and were found to be 38.6, 9.5, and 42.3 nm for M53Fe, ZFO, and ZFO/M53Fe, respectively.

The FTIR spectra for the photocatalysts are presented in Fig. 4. M53Fe exhibits five major absorption peaks at 752, 1,014.6, 1,382, 1,524.51, and 1,625 cm^{-1} that were attributed to the dicarboxylate linker. The peaks at 752 and 3,042 represent C-H bond vibration in benzene aromatic ring [50,51]. The low intensity peak at 1,625 cm^{-1} is attributed to C=O bond and the two sharp and peaks at 1,382 cm^{-1} and 1,524 cm^{-1} are attributed to asymmetric vibration and symmetric vibrations of carboxyl groups, respectively, confirming the existence of phthalic acid linker in M53Fe and ZFO/M53Fe composite [26,39,52]. The FTIR spectrum of ZFO shows broad peaks at 1,338 and 1,542 cm^{-1} attributed to the characteristic absorption bond of -COO confirming the presence of $Zn(Ac)_2$ on the surface of ZFO nanoparticle and the covalent bond between carboxylate group of acetate and zinc [52,53]. Furthermore, the peaks at 2,850 to 2,950 and at 1,000 to 1,100 cm^{-1} are related to antisymmetric C-H and C-O bonds, respectively [53-55]. Tetrahedral and octahedral metal oxide bonds (Zn-O and Fe-O) are attributed to absorption peaks in the range of 530-552 cm^{-1} [48,56]. Moreover, the vast broadband in the range of 3,400 to 3,600 cm^{-1} was observed in all FTIR spectra and was assigned to the stretching mode of the O-H group of water molecules on the surface of the samples that maybe have remained after washing in the synthesis process [12,57-59].

The FE-SEM images for the synthesized photocatalysts are presented in Fig. 5, indicating that samples M53Fe and ZFO display like micro-rods and sphere-like shapes, respectively. The M53Fe stakes have a width of approximately 4 to 10 μm and length of several tens of micrometers. ZFO spheres have diameters ranging from 40 to 60 nm in accordance to evidence reported elsewhere in the literature [26,39,60]. The image for ZFO suggests that natural agglomeration had occurred. ZFO/M53Fe image indicates a broken edge stake with ZFO nanoparticles well dispersed evenly on the surface of M53Fe.

The results from EDX analysis for the photocatalysts are presented in Fig. 6, confirming the presence of C, O, and Fe in M53Fe. Additionally, the presence of Fe, O, and Zn was confirmed for ZFO with small amount of sodium from NaOH that was used for pH adjustment during the synthesis process [60]. The ZFO/M53Fe sample reveals the presence of the main elements, including Fe, Zn, O, and C.

Effortless separation of photocatalysts from the effluent stream is a desired characteristic for economical applications [61,62]. The magnetic properties of ZFO and ZFO/M53Fe were examined by vibrato sample magnetometry (VSM) analysis at room tempera-

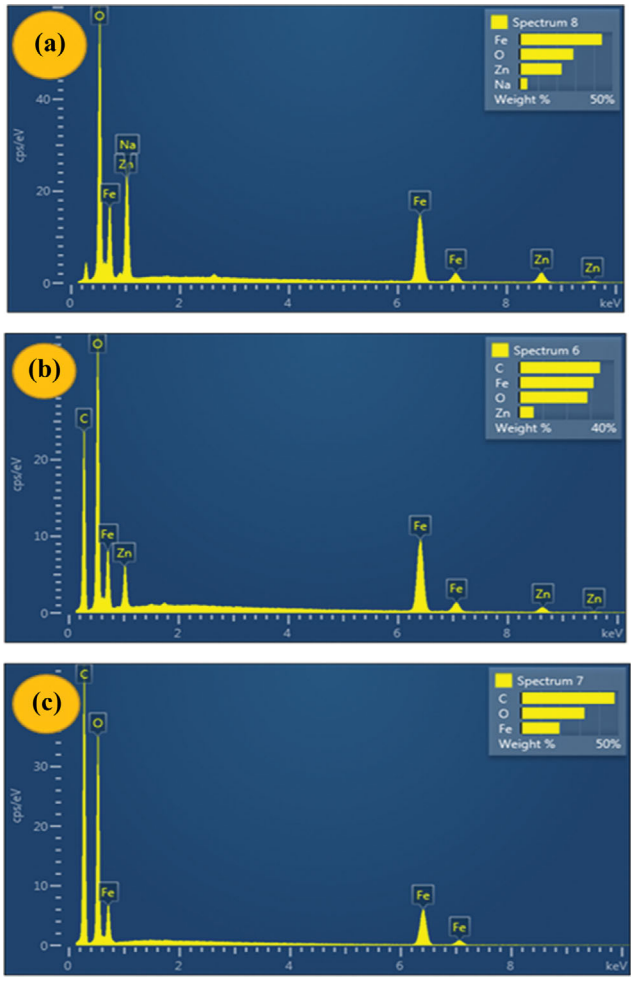

Fig. 6. Elemental analysis of photocatalysts: (a) ZFO, (b) ZFO/M53Fe, and (c) M53Fe.

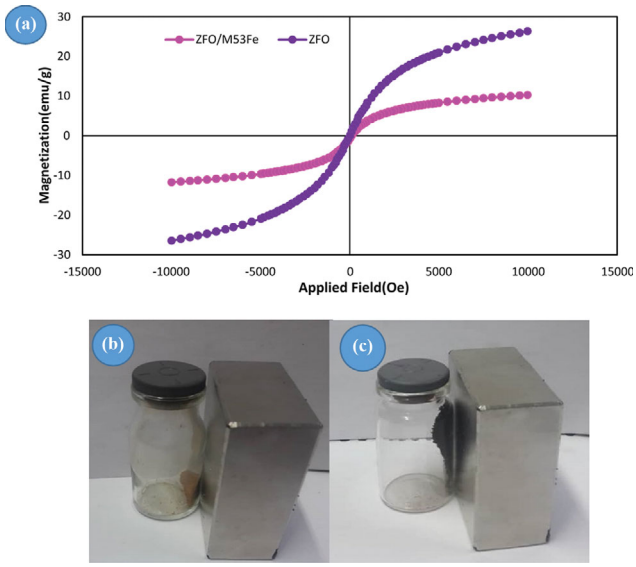

Fig. 7. Magnetization curves of pure ZFO and ZFO/M53Fe (a), and photographs of separation of the sample by a magnet for ZFO/M53Fe (b) and ZFO (c).

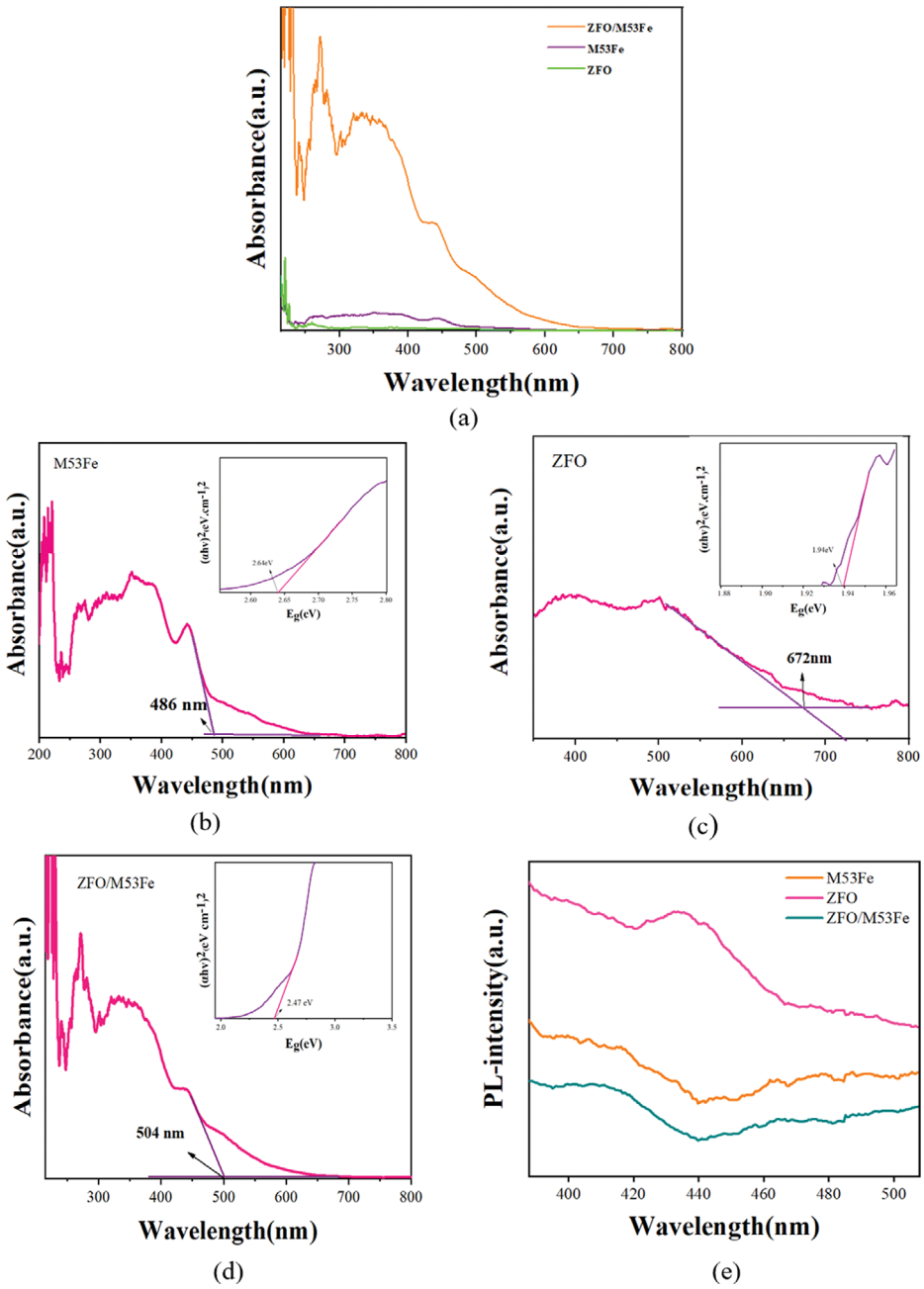

Fig. 8. Comparison of UV-vis/DRS analyses of the photocatalysts: (a) estimation of absorbance edge wavelength and bandgap, (b) M53Fe, (c) ZFO, (d) ZFO/M53Fe, and (e) photoluminance analyses.

ture. The applied magnetic field was from −15,000 to 15,000 Oe. The VSM results are presented in Fig. 7, illustrating that both photocatalysts did not reveal a hysteresis loop. They both had zero remanence (Mr=0) and coercivity (Hr=0), indicating superparamagnetic properties and a soft magnetic substance [19]. The related values for saturation magnetization of ZFO and ZFO/M53Fe were M_s=26.3 emu/g and M_s=10.23 emu/g at H=10.23 Oe, respectively [63,64]. ZFO/M53Fe has lower magnetic properties than ZFO due to a decrease in the amount of ZFO per unit mass of the composite. Figs. 7(b) and 7(c) illustrate photographs of ZFO/M53Fe and ZFO when exposed to a magnetic field, suggesting their easy recovery of them from a dye solution for subsequent recycling [64].

Optical features and absorption of the synthesized M53Fe and ZFO and their composite ZFO/M53Fe were probed by diffuse reflectance electromagnetic UV-visible spectra (DRS) analysis [65]. Fig. 8 indicates that the three photocatalysts have absorption in the range from 200 to 500 nm. ZFO has lower and weaker absorption intensity than the other two photocatalysts. ZFO/M53Fe has the highest absorption range in the UV-visible region [66,67]. The prominent absorption edges of M53Fe, ZFO and ZFO/M53Fe were around 471 nm, 672 nm, and 504 nm. The bandgap of crystalline photocatalyst was determined from the tangent line on the Tauc

plot [64,65] that was based on the Kulbelka-Munk Eq. (2):

$$\alpha h\nu = A(h\nu - Eg)^n \quad (2)$$

where α, hv and A represent absorption coefficient, photonic energy (eV), and proportionality constant. The value of n depends on the state of the optical transition materials, which is equal to 2 or 1/2 for the semiconductor (in this case, n=1/2 for direct transition) [49,67,68]. Ultimately, the horizontal axis of the plot was calculated by hv=1,240/λ with $(\alpha h\nu)^2$ as the vertical axis. The bandgap was obtained from the intersection of tangent along curves with the x-axis [68,69] and the values for bandgap energy for M53Fe, ZFO, and ZFO/M53Fe were estimated to be 2.64 eV, 1.94 eV, and 2.47 eV, respectively [34,39]. The band at 225 nm for M53Fe ZFO/M53Fe is related to the ligand-to-cluster charge transfer (LCCT) and inter ligand n-π and π-π transitions [43] of O(II)→Fe(III) that is ascribed to oxygen bond of carboxylate ligand to metal nodes or clusters [39,70]. In addition, a peak at about 471 nm appears for M53Fe, which may be due to the spin allowed transition d-d (6A1g=> 4A1g+4Eg(G)) of octahedral coordination (Fe^{3+}) in MOF [45,71]. The absorption edge of the ZFO/M53Fe is shifted to 504 nm as compared with M53Fe.

The separation and transition efficiency of photo-induced electron-hole pairs play a crucial role in the performance of semiconductors. The fluorescence intensity is affected by the irradiative recombination of charge carriers since the recombination of the photoexcited charge carrier is accompanied by the fluorescence emission. The lowest emission intensity generally illustrates a lower recombination rate of charge carriers,, thus leading to better photocatalytic activity [71]. As indicated in Fig. 8(e), the PL spectra of the ZFO after excitation at 355 nm exhibit the highest PL intensity and accordingly have the highest charge carrier recombination rate as it has a narrow bandgap (1.94 eV). On the other hand, ZFO/M53Fe displays the lowest PL intensity suggesting that it has the lowest recombination efficiency of photo-induced electron and hole pair [25,72]. The addition of M53Fe can effectively improve the separation of photo-induced carriers, which would lead to enhanced photocatalytic activity as compared with ZFO [73].

2. Photocatalytic Activity of Synthesized Catalysts

The photocatalytic activity of the synthesized catalysts in degradation of the Azo DR-23 dye is examined in this section. This degradation was carried out both in the presence and absence of the catalysts. A slight amount of dye degradation was observed when the pure dye solution without any catalysts was exposed to the light from the projector lamp for two hours, indicating slight self-degradation in the face of light. Subsequently, the experiment was carried out with 0.005 g of catalyst placed in 100 ml of dye solution at optimum pH of 3.1 followed by agitation in the dark for one hour to allow for the solution to reach adsorption-desorption equilibrium with the catalyst. As illustrated in Fig. 9, adsorption efficiency of ZFO, M53Fe, and ZFO/M53Fe was 25.3, 28.3, and 43.8%, respectively. The lamp was then turned on and the dye solution was allowed to remain under light for an additional 120 minutes. The dye removal efficiency was 49.16, 78.89, and 92.33% for ZFO, M53Fe, and ZFO/M53Fe, respectively, indicating a superior DR23 degradation efficiency for ZFO/M53Fe composite as compared with ZFO and MIL53 photocatalysts, as was suggested by the data from UV-Vis analyses [74]. Under visible light, electrons and holes can be generated by the bandgap radiation of catalysts. The generated holes in the VBM (valence band maximum) of the catalyst could eliminate DR-23 by direct oxidation. The minimum conduction band level with the self-formation of hydrogen peroxide can also cause further degradation of the chromophoric structure of the organic dye molecules. The heterogeneous junction of the two photocatalysts resulted in reduced recombination of electron-hole pairs, thus significantly improving photocatalytic performance.

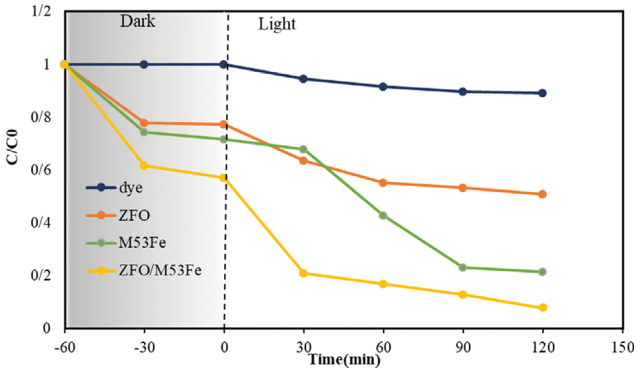

Fig. 9. Photocatalyst activity for DR-23 degradation (catalyst concentation: 50 mg/l, dye concentration: 10 ppm, pH=3.1, T=298 K).

3. Kinetics of Photocatalytic Degradation

Photocatalytic degradation rates depend on the nature of the active sites of the photocatalyst [75]. The reaction rate constant was calculated for the three photocatalysts in terms of zero-order, first-order, and second-order kinetic models. The calculated rate constants, k, and the corresponding correlation coefficient, R^2, are reported in Table 1 indicating that a second-order rate expression adequately describes the residual concentration of DR-23 dye with reaction time for all photocatalysts. Fig. 10 shows the results for the second-order, first-order and zero-order kinetics where C_0 is the initial concentration of DR-23, C is the concentration at time t and

Table 1. Comparison of kinetic models for degradation of DR-23 dye

Photocatalyst	Zero-order kinetics $C_0-C=-k_0t$		First-order kinetics $\ln(C_0/C)=k_1t$		Second order kinetics $(1/C)-(1/C_0)=k_2t$	
	R^2	k (mg/min l)	R^2	k (min^{-1})	R^2	k (l/mg·min)
M53Fe	0.9271	0.0484	0.936	0.0116	0.9024	0.0031
ZFO	0.8896	0.0211	0.889	0.0034	0.9178	0.0005
ZFO/M53Fe	0.74	0.0355	0.9205	0.015	0.9347	0.0085

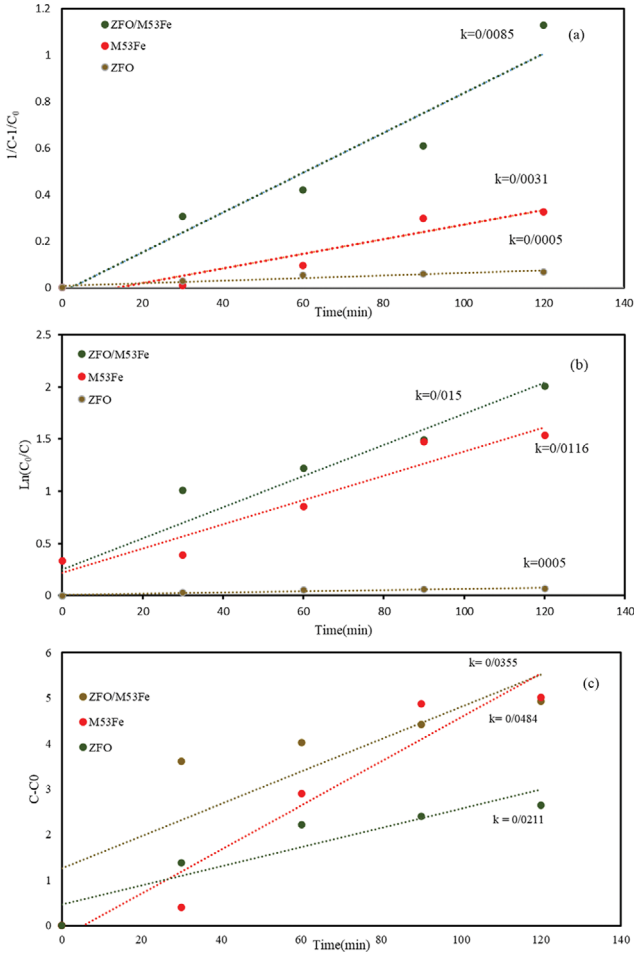

Fig. 10. Degradation of DR-23 in terms of (a) Second-order, (b) First-order kinetic models, (c) Zero-order.

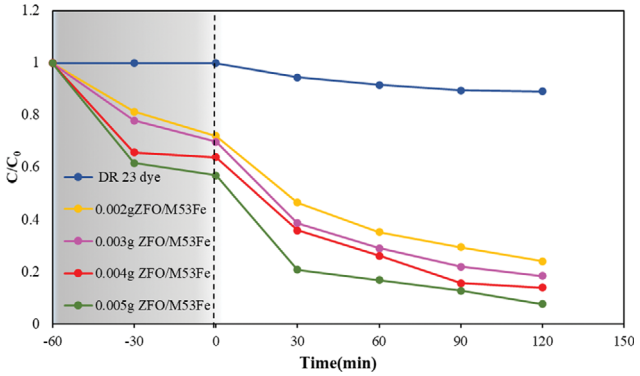

Fig. 11. Degradation of DR-23 with ZFO/M53Fe at different catalyst dosage (Initial DR-23 concentration: 10 mg/l, pH=3.1).

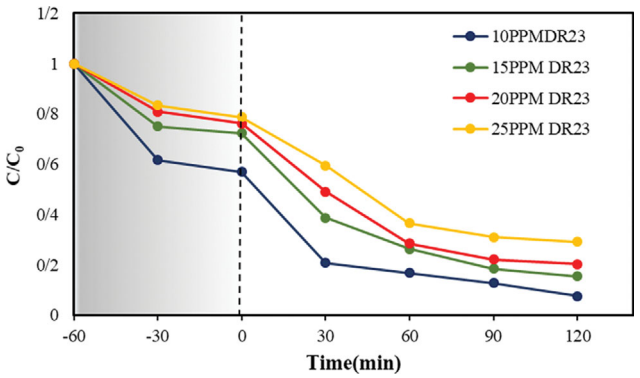

Fig. 12. Degradation of DR-23 by ZFO/M53Fe with different initial dye concentration (catalyst dosage: 50 mg/l, pH=3.1).

k is the apparent rate constant obtained from the slope with an acceptable correlation factor [45], indicating the highest rate constant for ZFO/M53Fe composite as compared with ZFO and M53Fe.

4. Effect of Catalyst Dosage

The photocatalyst dosage is an important factor influencing the degradation of DR-23. To obtain the optimal amount of photocatalyst, experiments were performed with catalyst loading of 2 mg to 5 mg in 100 ml of dye solution while keeping other operating parameters including pH, temperature, and initial dye concentration constant. As shown in Fig. 11, an increase in photocatalyst loading led to a corresponding increase in dye degradation. The increase in the degradation rates was due to a greater number of active catalytic sites producing more electron-hole pairs leading to greater concentration of radical species ($O_2^{\bullet}$, h^+, and $OH^{\bullet}$) in the dye solution and subsequently to increased decolorization [76-83].

5. Effect of Initial Dye Concentration

The influence of initial dye concentration on the degradation of DR-23 was explored using solutions containing from 10 to 25 mg/l of dye with ZFO/M53Fe as the photocatalyst, keeping other operating parameters, including photocatalyst dosage, temperature, and initial solution pH, constant. As indicated in Fig. 12, an increase in the initial dye concentration led to a decrease in photocatalytic activity since the penetration of light would decrease with increasing dye concentration.

6. Effect of Initial Solution pH

The solution pH is one of the most important and effective operating parameters in dye degradation as it influences the rate of adsorption and desorption of dye molecules on the catalyst surface and also affects the potential of valance band and physicochemical properties of the catalyst surface. Fig. 13 illustrates the extent of dye degradation by ZFO/M53Fe composite at different pH values that were adjusted by addition of NaOH 1 M and HCl 1 M dilute solutions, indicating that degradation of the anionic dye had decreased with increasing pH. The highest degradation efficiency has been reported for acidic solution (pH=3.1).

The catalyst surface charge also depends on the solution pH. There was a significant difference in the amount of anionic dye adsorption by the composite at pH=3.1 as compared with other pH values. This is attributed to the electrostatic repulsion of opposite charges on catalyst surface (positive charge) in acidic solution and anionic dye. The produced OH^- ions combine with the H^+ ions on the photocatalyst surface under alkaline conditions, thus reducing the adsorption efficiency. The lower degradation rate of DR-23 at higher pH values could also be related to the lower oxidation potential of •OH at a higher pH (2.8 V at pH=0 compared with 1.9 V at pH=7: 1.9 V) [74].

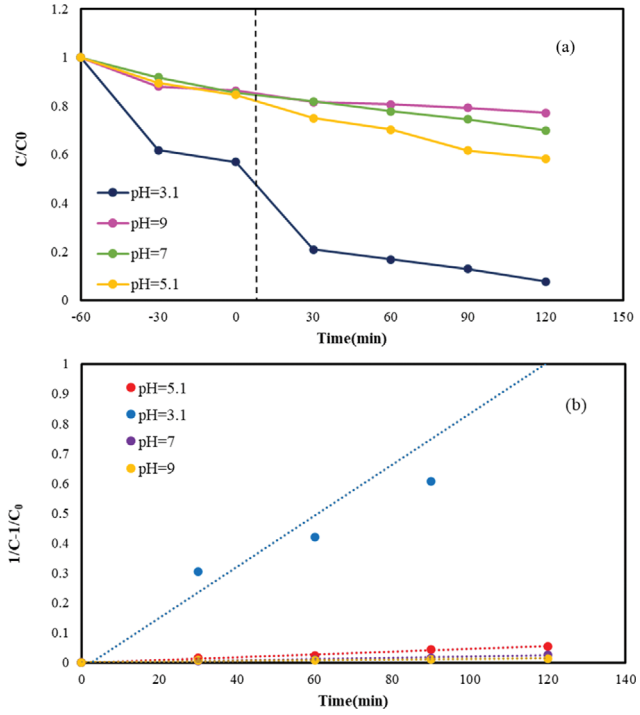

Fig. 13. (a) Degradation of DR-23 at different pH (b) second-order kinetic analysis.

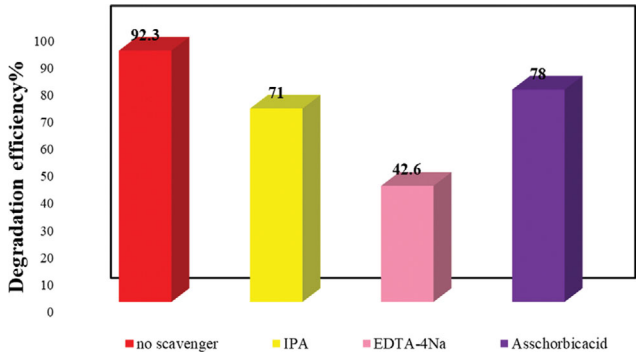

Fig. 14. Quenching tests with and without scavenger agents (catalyst dosage: 0.5 g/l, initial concentration of DR-23: 10 mg/l, pH=3.1 (adjusted), T=298 K).

7. Free Radical Species Quenching Test

Trapping of free radical species is a facile method to detect active species produced in dye decomposition by an advanced oxidizing process. Ethylene diamine tetra acetic acid tetrasodium salt (EDTA-4Na, h^+ trapping), L-ascorbic acid (O_2^- trapping) [57], isopropanol (•OH trapping), and Na_2SO_4 (electron trapping) were added separately to 10 ppm DR-23 aqueous solution at pH=3.1. The results of the scavenger tests using ZFO/M53Fe composite as the photocatalyst are presented in Fig. 14. The decrease in degradation efficiency was more significant with the addition of 2-propanol (IPA) and (EDTA-4Na) as compared with the addition of ascorbic acid and sodium sulfate into solution. Although electrons are considered to play only a small role in the degradation of dye, their role is still important and their effectiveness is similar to the role of superoxide oxygen produced by the reaction of oxygen with electrons in solution. The scavenger test results confirmed that the principal active species in photocatalytic degradation of DR-23 are •OH and h^+ (photo-generated holes).

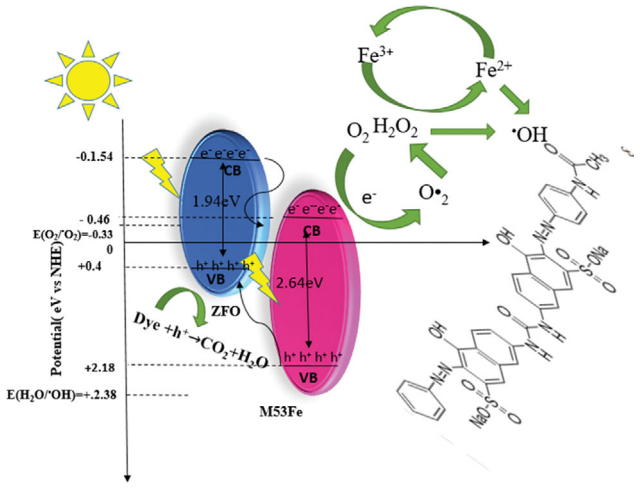

Fig. 15. Proposed reaction mechanism for photocatalytic degradation of DR-23.

8. Proposed Photocatalytic Mechanism for DR-23 Degradation

With ZFO having a narrow bandgap (1.94 eV), the recombination of electron-hole pair rate is extremely fast. The separation of photo-generated electron-hole is vital for efficient photocatalytic activity. A possible charge transfer mechanism for ZFO/M53Fe hetero structure photocatalytic system is illustrated in Fig. 15. Electrons receive energy and migrate from the HOMO band of the semiconductors to their LUMO level by irradiating visible light on the photocatalytic surface. The CB of ZFO (−1.54 eV vs. NHE) [23, 84,85] is more negative than CB of M53Fe (−0.46 eV vs. NHE) [26]. The photo-generated electrons on the CB of ZFO can rapidly transfer to the CB of M53Fe. At the same time, a hole is generated inside their valence band. The energy level of the valence band (EVB) can be determined as EVB=ECB+Eg where Eg is the bandgap energy obtained from the DRS analysis. The bandgap of ZFO and M53Fe was determined to be 1.94 eV and 2.64 eV and, consequently, their valance band levels were calculated to be +0.4 eV and +2.18 eV, respectively.

The valance band level of M53Fe is lower than the valance band of ZFO. The holes produced in M53Fe migrate to the valence layer on the spinel Zinc ferrite since the standard redox potential of ($•OH/H_2O$) (2.38 eV vs. NHE) [28] is lower than the ZFO valance band level. The holes in ZFO combine directly with the dye molecules, leading to their destruction and breaking of their bonds and thereby starting radical chain oxidation (reaction 4), which is in agreement with trapping experiments [29].

$$\text{Iron-based catalysts}+hv \rightarrow e^- + h^+ \quad (3)$$

$$h^+ + RH \rightarrow R^\bullet + H^+ \quad (4)$$

Since the conduction band of ZFO is more negative than the potential of the M53Fe conduction band, the excited electrons could be transferred from ZFO to the M53Fe, resulting in an efficient sepa-

ration between electrons and holes [84]. Furthermore, the conduction band of M53Fe (−0.46 eV vs. NHE) is more negative than the reduction potential of $O_2/O_2^{\bullet-}$ (−0.33 eV vs. NHE) [73,83]. The electrons can react with surface chemisorbed oxygen and form anion superoxide radicals (Reaction 8) that, along with hydroxyl radicals, leads to the destruction of the dye structure (reactions 5-10).

$$O_2+e^- \rightarrow {}^{\bullet}O_2^- \quad (5)$$

$${}^{\bullet}O_2^-+H^+ \rightarrow HOO^{\bullet} \quad (6)$$

$$HOO^{\bullet}+e^- \rightarrow HOO^- \quad (7)$$

$$HOO^-+H^+ \rightarrow H_2O_2 \quad (8)$$

$$H_2O_2+e^- \rightarrow {}^{\bullet}OH+OH^- \quad (9)$$

$${}^{\bullet}OH/O_2^-/h^++R \rightarrow \text{several steps} \rightarrow CO_2+H_2O \quad (10)$$

If there is a sufficient amount of reactive species in the solution, the final reaction products will be carbon dioxide and water (reaction 13). The results indicate that ZFO/M53Fe was a heterojunction type-II [85,86] that had a high photocatalytic activity for degradation of DR-23 with hydroxyl radicals and photogenerated holes on the surface as the key reagents in the photodegradation mechanism [84].

9. Reusability of Photocatalysts

Photocatalytic degradation by various photocatalysts is one of the most important processes in removing pollutants [87-90]. The long-term reusability of a photocatalyst is crucial for large-scale applications. Fig. 16 shows the degradation efficiency of ZFO/M53Fe in five consecutive cycles for photodegradation of a 10 ppm solution of DR-23 at pH=3.1 and 0.5 g/L catalyst loading. After each photodegradation experiment, the photocatalysts were collected by an external magnet and washed with ethanol and distilled water, and subsequently dried in an oven at 60 °C. The results indicate only a small loss in photocatalytic activity. Fig. 17 indicated that the synthesized photocatalyst had high stability because the XRD pattern before and after photocatalytic degradation process did not change significantly.

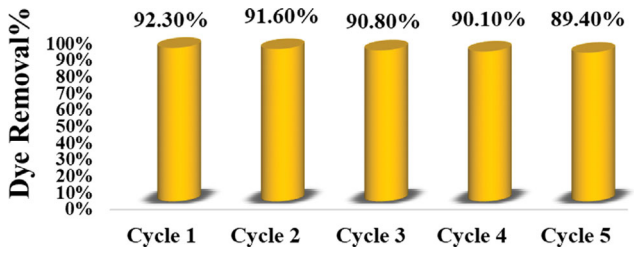

Fig. 16. Degradation of DR-23 after 5 cycles using ZFO/M53Fe.

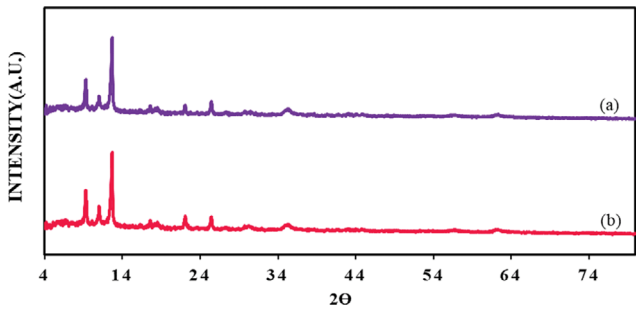

Fig. 17. XRD pattern of ZFO/M53Fe magnetic composite (a) after and (b) before photocatalytic degradation process.

CONCLUSION

Magnetically separable ZFO/M53Fe composite was synthesized using a solvothermal method for DR-23 degradation using a visible light source. The XRD analyses confirmed the successful formation of crystalline phases related to ZFO and M53Fe in the ZFO/M53Fe heterojunction composite. SEM images of ZFO/M53Fe showed that the sphere-like ZFO magnetic nanoparticles were well-dispersed on the surface of M53Fe micro-rod structures. The photocatalytic activity of the composite was superior as compared with ZFO and M53Fe and nearly maintained its activity after five consecutive cycles. The present novel composite design provides an ideal approach for the synthesis of magnetic nanoparticles such as ZFO to obtain high activity, stability, and magnetic recyclability for photocatalytic dye degradation.

REFERENCES

1. N. M. Mahmoodi and S. Soltani-Gordefaramarzi. *Prog. Color Colorants Coat.*, **9**, 85 (2016).
2. D. Asefi, N. M. Mahmoodi and M. Arami. *Colloids Surf. A: Physicochem. Eng. Asp.*, **355**, 183 (2010).
3. N. M. Mahmoodi and M. Arami, *J. Appl. Polym. Sci.*, **109**, 4043 (2008).
4. N. M. Mahmoodi, *J. Ind. Eng. Chem.*, **20**, 2050 (2014).
5. S. Davarpanah, N. M. Mahmoodi, M. Arami, H. Bahrami and F. Mazaheri, *Appl. Surf. Sci.*, **255**, 4171 (2009).
6. N. M. Mahmoodi, *J. Taiwan Instit. Chem. Eng.*, **45**, 2008 (2014).
7. N. M. Mahmoodi and F. Najafi, *Micropor. Mesopor. Mater.*, **156**, 153 (2012).
8. N. M. Mahmoodi, M. Arabloo and J. Abdi, *Water Res.*, **67**, 216 (2014).
9. N. M. Mahmoodi, *J. Mole. Catal. A: Chem.*, **366**, 254 (2013).
10. N. M. Mahmoodi, M. Arami and J. Zhang, *J. Alloys Compd.*, **509**, 4754 (2011).
11. N. M. Mahmoodi, M. Arami, N. Y. Limaee, K. Gharanjig and F. Nourmohammadian, *Mater. Res. Bull.*, **42**, 797 (2007).
12. Q. Zhang, L. Jiang, J. Wang, Y. Zhu, Y. Pu and W. Dai, *Appl. Catal. B Environ.*, **277**, 119122 (2020).
13. G. Mamba and A. K. Mishra, *Appl. Catal. B Environ.*, **198**, 347 (2016).
14. W. Zhao, C. Liang, B. Wang and S. Xing, *ACS Appl. Mater. Interface*, **9**, 41927 (2017).
15. M. Chen, Y. Dai, J. Guo, H. Yang, D. Liu and Y. Zhai, *Appl. Surf. Sci.*, **493**, 1361 (2019).
16. C. Sambathkumar, S. E. Arasi, B. Natarajan, A. Arivarasan and P. Devendran, *Int. J. Eng. Adv. Technol.*, **9**, 1085 (2019).
17. M. Kuang, J. Zhang, W. Wang, J. Chen, R. Liu, S. Xie, J. Wang and Z. Ji, *Solid State Sci.*, **96**, 105901 (2019).
18. J. Su, Q. Shang, T. Guo, S. Yang, X. Wang, Q. Ma, H. Guan, F. Xu

and S. C. Tsang, *Mater. Chem. Phys.*, **219**, 22 (2018).
19. T. Xie, L. Xu, C. Liu and Y. Wang, *Appl. Surf. Sci.*, **273**, 684 (2013).
20. E. Erusappan, S. Thiripuranthagan, M. Durai, S. Kumaravel and T. Vembuli, *New J. Chem.*, **44**, 7758 (2020).
21. Y. Yao, Y. Cai, F. Lu, J. Qin, F. Wei, C. Xu and S. Wang, *Ind. Eng. Chem. Res.*, **493**, 17294 (2014).
22. J. P. Dhal, B. G. Mishra and G. Hota, *RSC Adv.*, **5**, 58072 (2015).
23. Z. Wang, C. Lai, L. Qin, Y. Fu, J. He and D. Huang, *Chem. Eng. J.*, **392**, 124851 (2020).
24. S. Zhang, Y. Xu, D. Zhao, W. Chen, H. Li and C. Hou, *Molecules*, **25**, 124 (2020).
25. Y. Gao, S. Li, Y. Li, L. Yao and H. Zhang, *Appl. Catal. B Environ.*, **202**, 165 (2017).
26. K. Y. Andrew Lin, H. A. Chang and C. J. Hsu, *RSC Adv.*, **5**, 32520 (2015).
27. J. J. Du, Y. P. Yuan, J. X. Sun, F. M. Peng, X. Jiang, L. G. Qiu, A. J. Xie, Y. H. Shen and J. F. Zhu, *J. Hazard. Mater.*, **190**, 945 (2011).
28. Q. Liu, C. Zeng, L. Ai, Z. Hao and J. Jiang, *Appl. Catal. B Environ.*, **224**, 38 (2018).
29. J. Su, S. Yuan, H. Y. Wang, L. Huang, J. Y. Ge, E. Joseph, J. Qin, T. Cagin, J. L. Zuo and H. C. Zhou, *Nat. Commun.*, **8**, 1 (2017).
30. E. J. Carrington, C. A. McAnally, A. J. Fletcher, S. P. Thompson, M. Warren and L. Brammer, *Nat. Chem.*, **9**, 882 (2017).
31. F. Millange, N. Guillou, M. E. Medina, G. Férey, A. Carlin-Sinclair, K. M. Golden and R. I. Walton, *Chem. Mater.*, **22**, 4237 (2010).
32. J. Du, Y. Yuan, J. Sun, F. Peng, X. Jiang and L. Qiu, *J. Hazard. Mater.*, **190**, 945 (2011).
33. R. Panda, S. Rahut and J. K. Basu, *RSC Adv.*, **6**, 80981 (2016).
34. O. Abida, M. Kolar, J. Jirkovsky and G. Mailhot, *Photochem. Photobiol. Sci.*, **11**, 794 (2012).
35. Z. Wang, X. Chen, H. Ji, W. Ma, C. Chen and J. Zhao, *Environ. Sci. Technol.*, **44**, 263 (2010).
36. H. Park, H. I. Kim, G. H. Moon and W. Choi, *Energy Environ. Sci.*, **9**, 411 (2016).
37. P. Hu, C. Chen, J. Song and Z. Tang, *Mater. Sci. Semicond. Process.*, **77**, 40 (2018).
38. C. Zhang, L. Ai and J. Jiang, *J. Mater. Chem. A.*, **3**, 3074 (2015).
39. J. Xiao, W. Yang, S. Gao, C. Sun and Q. Li, *J. Mater. Sci. Technol.*, **34**, 2331 (2018).
40. S. Ghimire, M. Flury, E. J. Scheenstra and C. A. Miles, *Sci. Total Environ.*, **703**, 135577 (2019).
41. L. Hu, G. Deng, W. Lu, S. Pang and X. Hu, *Appl. Surf. Sci.*, **410**, 401 (2017).
42. R. Bayat, P. Derakhshi, R. Rahimi, A. A. Safekordi and M. Rabbani, *Solid State Sci.*, **89**, 167 (2019).
43. T. Araya, M. Jia, J. Yang, P. Zhao, K. Cai, W. Ma and Y. Huang, *Appl. Catal. B Environ.*, **203**, 768 (2017).
44. R. Liang, F. Jing, L. Shen, N. Qin and L. Wu, *J. Hazard. Mater.*, **287**, 364 (2015).
45. S. D. Kulkarni, S. Kumbar, S. G. Menon, K. S. Choudhari and C. Santhosh, *Mater. Res. Bull.*, **77**, 70 (2016).
46. A. S. Munn, A. J. Ramirez-Cuesta, F. Millange and R. I. Walton, *Chem. Phys.*, **427**, 30 (2013).
47. H. Chen, Y. Liu, T. Cai, W. Dong, L. Tang, X. Xia, L. Wang and T. Li, *ACS Appl. Mater. Interface*, **11**, 28791 (2019).
48. A. Behera, D. Kandi, S. M. Majhi, S. Martha and K. Parida, *Beilstein J. Nanotechnol.*, **9**, 436 (2018).
49. X. Feng, H. Chen and F. Jiang, *J. Colloid Interface Sci.*, **494**, 32 (2017).
50. V. H. Nguyen, L. G. Bach, Q. T. P. Bui, T. D. Nguyen, D. V. N. Vo, H. T. Vu and S. T. Do, *J. Environ. Chem. Eng.*, **6**, 7434 (2018).
51. A. A. Oladipo, *Process Saf. Environ. Prot.*, **116**, 413 (2018).
52. J. Feng, Z. Zhang, M. Gao, M. Gu, J. Wang, W. Zeng, Y. Lv, Y. Ren, Z. Fan, H. Zhao, R. Liu, Q. Zhang and Q. Wang, *Mater. Res. Bull.*, **223**, 172 (2019).
53. H. Zhao, R. Liu, Q. Zhang and Q. Wang, *Mater. Res. Bull.*, **75**, 172 (2016).
54. P. R. Matli, X. Zhou, D. Shiyu and Q. Huang, *Int. Nano Lett.*, **5**, 53 (2015).
55. A. R. Abbasian and M. S. Afarani, *Appl. Phys. A Mater. Sci. Process.*, **125**, 721 (2019).
56. J. Feng, Z. Zhang, M. Gao, M. Gu, J. Wang, W. Zeng, Y. Lv, Y. Ren and Z. Fan, *Mater. Chem. Phys.*, **223**, 758 (2019).
57. S. B. Bagherzadeh, M. Kazemeini and N. M. Mahmoodi, *J. Mol. Liq.*, **19**, 35661 (2020).
58. D. Wang, F. Jia, H. Wang, F. Chen, Y. Fang, W. Dong, G. Zeng, X. Li, Q. Yang and X. Yuan, *J. Colloid Interface Sci.*, **519**, 273 (2018).
59. C. Zhang, L. Ai and J. Jiang, *Ind. Eng. Chem. Res.*, **54**, 153 (2015).
60. S. Borthakur and L. Saikia, *J. Environ. Chem. Eng.*, **7**, 103035 (2019).
61. P. liang Liang, L. Yong Yuan, H. Deng, X. Cong Wang, L. Wang, Z. Jie Li, S. Zhong Luo and W. Q. Shi, *Appl. Catal. B Environ.*, **267**, 118688 (2020).
62. Y. Sun, J. Lei, Y. Wang, Q. Tang and C. Kang, *RSC Adv.*, **10**, 17293 (2020).
63. A. A. Oladipo, A. O. Ifebajo and M. Gazi, *Appl. Catal. B Environ.*, **243**, 243 (2019).
64. J. Liu, G. Liu, C. Yuan, L. Chen, X. Tian and M. Fang, *New J. Chem.*, **42**, 3736 (2018).
65. J. Yang, X. Niu, S. An, W. Chen, J. Wang and W. Liu, *RSC Adv.*, **7**, 2943 (2017).
66. Q. Wu, H. Yang, L. Kang, Z. Gao and F. Ren, *Appl. Catal. B Environ.*, **263**, 118282 (2020).
67. S. B. Rawal, H. J. Kang, D. I. Won and W. I. Lee, *Appl. Catal. B Environ.*, **256**, 117856 (2019).
68. H. Xiao, W. Zhang, Q. Yao, L. Huang, L. Chen, B. Boury and Z. Chen, *Appl. Catal. B Environ.*, **244**, 719 (2019).
69. M. Ahmad, S. Chen, F. Ye, X. Quan, S. Afzal, H. Yu and X. Zhao, *Appl. Catal. B Environ.*, **245**, 428 (2018).
70. G. T. Vuong, M. H. Pham and T. O. Do, *CrystEngComm.*, **15**, 9694 (2013).
71. N. K. Veldurthi, N. K. Eswar, S. A. Singh and G. Madras, *Catal. Sci. Technol.*, **8**, 1083 (2018).
72. Z. Yang, X. Xu, X. Liang, C. Lei, Y. Wei, P. He, B. Lv, H. Ma and Z. Lei, *Appl. Catal. B Environ.*, **198**, 112 (2016).
73. M. Wang, L. Yang, J. Yuan, L. He, Y. Song, H. Zhang, Z. Zhang and S. Fang, *RSC Adv.*, **8**, 12459 (2018).
74. C. Gao, S. Chen, X. Quan, H. Yu and Y. Zhang, *J. Catal.*, **356**, 125 (2017).
75. T. B. Nguyen and R. A. Doong, *RSC Adv.*, **7**, 50006 (2017).
76. N. M. Mahmoodi and M. Arami, *Chem. Eng. J.*, **146**, 189 (2009).
77. N. M. Mahmoodi, A. Taghizadeh, M. Taghizadeh and J. Abdi, *J. Hzard. Mater.*, **378**, 120741 (2019).
78. M. Oveisi, N. M. Mahmoodi and M. A. Asli, *J. Cleaner Prod.*, **222**,

669 (2019).
79. N. M. Mahmoodi, *Water Air Soil Pollut.*, **224**, 1612 (2013).
80. M. Oveisi, M. A. Asli and N. M. Mahmoodi, *Inorg. Chim. Acta*, **487**, 169 (2019).
81. N. M. Mahmoodi, *Environ. Monit. Assess.*, **186**, 5595 (2014).
82. N. M. Mahmoodi, M. Bashiri and S. J. Moeen, *Mater. Res. Bull.*, **47**, 4403 (2012).
83. N. M. Mahmoodi, J. Abdi, M. Taghizadeh, A. Taghizadeh, B. Hayati, A. A. Shekarchi and M. Vossuoghi, *J. Environ. Manage.*, **233**, 660 (2019).
84. S. Ruan, W. Huang, M. Zhao, H. Song and Z. Gao, *Mater. Sci. Semicond. Process.*, **107**, 104835 (2020).
85. J. Low, J. Yu, M. Jaroniec, S. Wageh and A. A. Al-Ghamdi, *Adv. Mater.*, **29**, 1 (2017).
86. R. Marschall, *Adv. Funct. Mater.*, **24**, 2421 (2014).
87. N. M. Mahmoodi, *Desalin. Water Treat.*, **53**, 84 (2015).
88. N. M. Mahmoodi, *J. Environ. Eng.*, **139**, 1368 (2013).
89. N. M. Mahmoodi, N. Y. Limaee, M. Arami, S. Borhany and M. Mohammad-Taheri, *J. Photochem. Photobiol. A: Chem.*, **189**, 1 (2007).
90. N. M. Mahmoodi, M. Arami, N. Y. Limaee, K. Gharanjig and F. D. Ardejani, *Colloids Surf. A: Physicochem. Eng. Asp.*, **290**, 125 (2006).